Nitric Oxide Dynamics in Truncated Hemoglobin: Docking Sites, Migration Pathways, and Vibrational Spectroscopy from Molecular Dynamics Simulations

Sabyashachi Mishra and Markus Meuwly*
Department of Chemistry, University of Basel, Basel, Switzerland

ABSTRACT Atomistic simulations of nitric oxide (NO) dynamics and migration in the trHbN of *Mycobacterium tuberculosis* are reported. From extensive molecular dynamics simulations (48 ns in total), the structural and energetic properties of the ligand docking sites in the protein have been characterized and a connectivity network between the ligand docking sites has been built. Several novel migration and exit pathways are found and are analyzed in detail. The interplay between a hydrogen-bonding network involving residues Tyr^{33} and Gln^{58} and the bound O_2 ligand is discussed and the role of Phe^{62} residue in ligand migration is examined. It is found that Phe^{62} is directly involved in controlling ligand migration. This is reminiscent of His^{64} in myoglobin, which also plays a central role in CO migration pathways. Finally, infrared spectra of the NO molecule in different ligand docking sites of the protein are calculated. The pocket-specific spectra are typically blue-shifted by 5–10 cm^{-1}, which should be detectable in future spectroscopic experiments.

INTRODUCTION

In recent years, the microbial hemoglobins (Hbs) have received much attention due to their wide range of functions in microorganisms (1,2). Three groups of Hbs have been identified in microorganisms, namely, flavohemoglobins (FHbs), single domain Hbs, and truncated Hbs (trHbs) (3). The FHbs contain a globin domain with a classical three-over-three α-helical structure and an additional flavin-containing reductase domain covalently attached to it. While the single domain Hbs share high sequence and structure homology with the globin domain of the FHbs, the trHbs, on the other hand, are much smaller with $\approx$110–140 amino-acid residues and exhibit a two-over-two α-helical structure (3–10).

The trHbs are phylogenetically divided into three groups—group I (trHbN); group II (trHbO); and group III (trHbP) (3)—which are 20–40 amino-acids shorter than the mammalian Hbs due to the presence of several shortened α-helices in trHbs. However, the residue deletions, insertions, and replacements relative to the vertebrate globin sequences are distributed throughout the globin chain. The trHbs host the heme in a two-over-two α-helical sandwich based on four helices, corresponding to the B, E, G, and H helices of the classical globin fold. The B/E and G/H helix pairs run antiparallel and surround the heme group to keep the latter safe from solvents. As compared to the classic globin fold, the trHbs show a drastically shortened A helix (absent in some cases, e.g., group III trHb). The D helix of classic globin fold is usually absent and the proximal F helix is almost completely replaced by an extended pre-F helix. The stabilization in the shortened helices to build a properly structured heme crevice is provided by three glycine-based motifs in group I and II trHbs (7).

Pesce et al. (10) and Milani et al. (11,12) have analyzed the crystal structures of several group I trHbs, including the crystal structure of group I trHb of *Mycobacterium tuberculosis*, which is the primary focus of this work. One in every three human beings in today's population is latently infected by *M. tuberculosis* (13,14), the causative agent of tuberculosis. It is now widely believed that the microorganism overcomes the toxicity of nitric oxide (NO) by converting it to harmless nitrates (15,16).

The trHbN of *M. tuberculosis* has a dimeric assembly. The dimer has an elongated shape, positioning the two hemes 22 Å apart. The interface area between two trHbN chains is ~310 $Å^2$ (11). The crystal structure reveals the presence of an almost continuous tunnel through the protein matrix connecting the heme distal pocket to the protein surface at two distinct sites (11). The tunnel is composed of two orthogonal branches, stretching 20 Å and 8 Å from the respective access sites to the heme ligand site, and has a diameter of 5–7 Å, thus covering a volume of $\approx$330–360 $Å^3$ (11). The crystal structure of trHbN with Xe atoms under pressure shows eight Xe atoms with different occupancy levels, three of which fall in the shorter branch of the tunnel and two in the longer branch of the tunnel (12).

There have been a number of experimental studies devoted to the spectroscopic aspects of several diatomic ligands (CO, O_2, NO, and CN) binding to the trHbN in *M. tuberculosis* (15,17–20). These authors have studied several mutants of the wt-trHbN and have proposed that the ligand binding is largely controlled by a pair of interacting amino acids (Gln^{58} and Tyr^{33}) in the heme active site by participating

Submitted September 26, 2008, and accepted for publication November 18, 2008.

*Corresponding m.meuwly@unibas.ch

Editor: Gregory A. Voth.

0006-3495/09/03/2105/14 $2.00

doi: 10.1016/j.bpj.2008.11.066

in H-bonding with the heme-bound diatomic O_2 ligand. In addition to the spectroscopic investigations, there exist several kinetic studies on ligand binding to trHbN (9). In trHbN, the O_2 binding is faster by a factor of two compared to sperm whale Mb whereas O_2 dissociation is two-orders-of-magnitude slower in trHbN, due to the presence of a tunnel in the trHbN for a faster ligand diffusion to the heme active site and the presence of ligand stabilizing residue Tyr^{33} (15). It has also been shown that the ligand binding is much faster in group I trHbs compared to the group II trHbs, which lack a tunnel for ligand diffusion (5).

Nitric oxide has been found to play a pivotal role in various physiological processes such as neurotransmission, regulation of vasodilation, inhibition of mitochondrial respiration, and immune response to bacterial infection (21,22). Overproduction of NO is potentially toxic (23). Important biological functions of NO involve its interaction with metal centers of heme and other metal-containing proteins (24). Additionally, nitric oxide is also known to participate in the reaction with superoxide to form peroxynitrite, the moiety that triggers several reactions such as lipid peroxidation, DNA damage, or thiol oxidization (25). For heme proteins, NO is a special ligand as it binds to both ferrous and ferric iron on the picosecond timescale in a variety of proteins including nitric oxide synthetase, guanylate cyclase, hemoglobin, and myoglobin (24,26).

From crystallographic studies, it is proposed that residue Phe^{62} exists in two conformations. In one, the benzene side chain of the residue blocks the longer channel of the tunnel path (the so-called closed state) and in the other it does not (the open state) (11,12). By long MD simulations (0.1 μs), Bidon-Chanal et al. have proposed that in deoxy-trHbN, the Phe^{62} adopts the closed conformation and hence the O_2 ligand enters the protein via the short channel. In case of oxygenated trHbN, the Phe^{62} prefers the open conformation, thus facilitating the entrance of the second ligand (NO) via the long channel (27,28).

The active sites of heme proteins are often buried inside the globin chain, which prevents direct contact with solvent. Therefore, the ligand has to trace its way to the heme by traversing through the globin chain. The driving force underlying the ligand migration is commonly believed to be due to thermal fluctuations of the proteins (29). The migration pathways and ligand access sites are located in, most likely, evolutionarily optimized well-defined regions of proteins that can be identified with systematic experimental and computational efforts (30). With the development of time-dependent crystallographic methods, it is now possible to investigate the time evolution of the ligand distribution after flash photolysis of heme-bound ligand (31–34). While such experimental methods are yet to be used routinely, computer simulations have complemented our understanding of ligand migration pathways, for example, in myoglobins by the so-called ligand implicit sampling method (35). In ligand implicit sampling, locating ligand migration pathways is based on a free-energy perturbation approach applied to simulations of the dynamical fluctuations of the protein in the absence of a ligand. The method provides complete three-dimensional maps of the potential of mean force for ligand placement anywhere in the protein. By using this method, several novel possible exit pathways have been suggested for myoglobin (35). The idea underlying potential of mean force-based implicit ligand sampling is the fact that diatomic ligands, often approximated as apolar, only interact weakly with the protein, and hence their impact on conformational changes of the protein are approximated as a small perturbation or even neglected. This approximation is, however, vulnerable when the ligand is either charged or possesses significant higher multipole moments, as is the case for CN^- or NO. In such cases, an explicit ligand sampling of the protein is required.

It is well known that NO can rapidly diffuse through the protein matrix (36), can easily cross membranes (37), and has a small barrier to escape to the bulk solvent (38). Hence, it can be used as a probe to explore the interior of proteins, such as active site conformations, ligand docking sites, or solvent-accessible regions. Moreover, since the molecule has an appreciable dipole moment, the NO stretching frequency can also be used as a spectroscopic probe. Unfortunately, because of its weak absorption cross section and spectral overlap with the amide bands (when it is bound to ferrous heme), measuring the NO stretching vibration has always remained a challenging experimental problem (39–42). Under such circumstances, computational investigations of NO in the protein environment are of considerable interest (26,43).

In this work, we use the NO ligand as a structural and spectroscopic probe for the trHbN of *M. tuberculosis* and employ the recently developed three-point fluctuating charge model for NO (43) and a suitable Morse potential for the N-O bond. The three-point fluctuating charge model, obtained by fitting to high-level ab initio dipole and quadruple moments, provides an accurate description of the electrostatic interactions between the ligand and the protein environment by correctly describing the variation of the multipole moments of the ligand as a function of its bond length (43).

COMPUTATIONAL METHODS

The initial structure of the protein is the x-ray crystal structure (Protein Data Bank entry 1IDR) and only monomer A of this homodimeric protein is considered in this study. Hydrogen atoms are added and the internal coordinates are built by using the appropriate modules of the CHARMM program (44). The protein contains 131 amino-acid residues, a prosthetic heme group as well as O_2 and NO ligands. All histidine residues are treated as δ-protonated. The heme group is covalently bound to the N of residue His^{81} and the dioxygen molecule is ligated to the Fe^{II} atom of the heme group, while the NO ligand remains unbound. A water box with dimension $62.1 \times 52.8 \times 68.3$ $Å^3$ is used to solvate the protein. The water molecules are represented via the modified TIP3P potentials (45). The water box was heated and equilibrated for 50 ps at 300 K before the protein was solvated. After deleting the

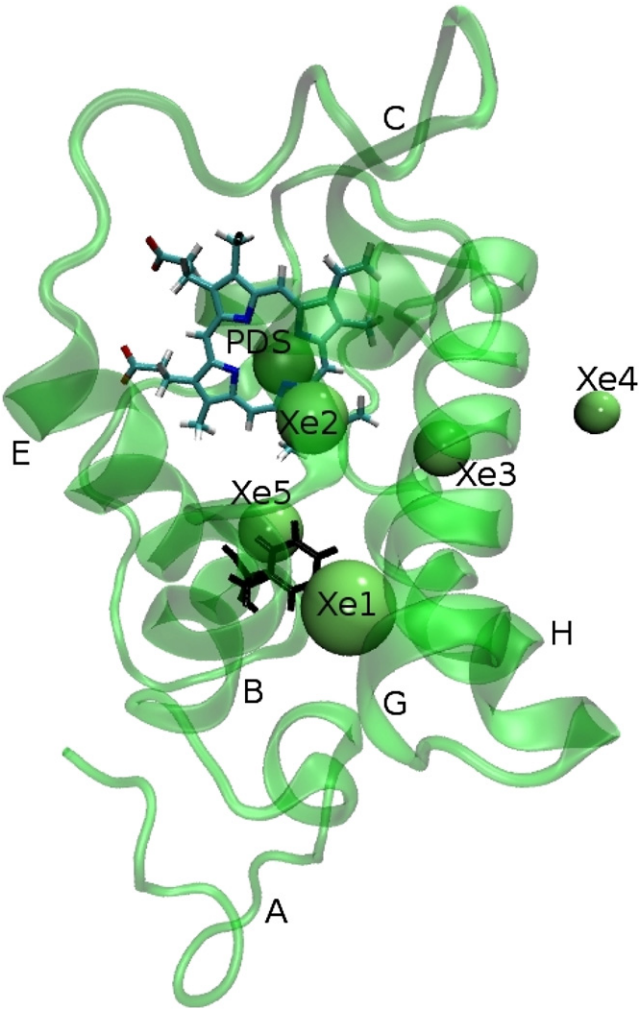

FIGURE 1 Ribbon representation of trHbN showing the structural elements. The heme group is shown with sticks and the ligand docking sites are shown by spheres. The docking sites are labeled according to the corresponding Xe pocket indices. The sphere-labeled PDS indicates the ligand docking site in the proximal side of the heme group, which is not seen in the crystallographic study of Milani et al. (11). The Phe[62] residue, which acts as a gate for ligand migration from Xe5 pocket to Xe1 pocket, is shown with black sticks.

water molecules overlapping the protein atoms, the simulation contains 6619 water molecules and the entire system has 21,975 atoms.

All MD simulations are carried out with the CHARMM22 force field (46) and the CHARMM program (44). Nonbonded interactions are truncated at a distance of 14 Å by using a shift function for the electrostatic terms and a switch algorithm for the van der Waals terms (47). All bonds involving hydrogen atoms are kept fixed by using SHAKE (48). The system was slowly heated to 300 K and equilibrated for at least 300 ps before free dynamics is performed at a constant temperature of 300 K. We have considered six starting structures of the protein by taking snapshots when the NO ligand is in one of the Xe1–Xe5 pockets and in the proximal docking site (PDS) (see Fig. 1 for the locations of the NO ligand in these *six snapshots*, represented by *spheres*). Four trajectories of 2-ns duration each were initiated from each of the six snapshots, which gives 24 trajectories each of 2-ns time length.

The recently developed three-point fluctuating charge model (43) for the dissociated NO molecule is used to describe the electrostatics of NO. All other interactions are treated with the CHARMM22 force field (46). The three-point fluctuating charge model is an improvement over the atom centered point-charge model in the sense that the latter are the 0[th] order expansion terms of the electrostatic potentials of the electron-density distribution. The expansion converges by considering the higher order expansion terms, which are essentially the higher order multipole moments of the ligand molecule. The charge model employed in this work is accurate up to the NO-quadrupole moment and thereby has the additional advantage of providing a more realistic description of the electrostatic interactions between the ligand and the protein environment. While the van der Waals parameters for the NO ligand are taken from Meuwly et al. (49), the N-O bond is described by a Morse potential,

TABLE 1 Force-field parameters for NO molecule

$V_{NO} = D_e(1 - \exp(-\beta(r - r_0)))^2$	$D_e = 152.6$ kcal/mol, $\beta = 2.636$ Å^{-1}, $r_0 = 1.151$ Å
$q_N = a_0 + a_1 r + a_2 r^2 + a_3 r^3$	$a_0 = -6.3$ e, $a_1 = 11.5$ eÅ^{-1}, $a_2 = -7.3$ eÅ^{-2}, $a_3 = 1.6$ eÅ^{-3}
$q_O = a_0 + a_1 r + a_2 r^2 + a_3 r^3$	$a_0 = -10.7$ e, $a_1 = 19.0$ eÅ^{-1}, $a_2 = -11.4$ eÅ^{-2}, $a_3 = 2.4$ eÅ^{-3}
$q_{CoM} = q_N + q_O$	
Nonbonded parameters (N)	$\varepsilon_N = 0.20$ kcal/mol, $r_N = 2.00$ Å
Nonbonded parameters (O)	$\varepsilon_O = 0.16$ kcal/mol, $r_O = 2.05$ Å

The Morse potential, the atomic (fluctuating) charges, and the nonbonded parameters (the van der Waals well depth ε and radii r) are taken from the literature (43,49,50), respectively.

$$V_M = D_e[1 - \exp(-\beta(r - r_e))]^2, \quad (1)$$

with dissociation energy $D_e = 152.6$ kcal/mol, $\beta = 2.636$ Å^{-1}, and equilibrium bond distance $r_e = 1.151$ Å (50). All force field parameters for the NO molecule are given in Table 1.

The free-energy profile along a progression coordinate (q) is estimated from the probability distribution $P(q)$ via the relation

$$\Delta G(q) = -k_B T \ln P(q), \quad (2)$$

where k_B is the Boltzmann constant (1.9875×10^{-3} kcal/mol/K) and T is the temperature in Kelvin.

The infrared absorption spectrum of the NO molecule is calculated by using the relation

$$A(\omega) = \omega\left[1 - \exp\left(-\frac{\hbar\omega}{k_B T}\right)\right] C(\omega), \quad (3)$$

where $C(\omega)$ is the Fourier transform of the dipole-dipole autocorrelation function,

$$C(t) = \frac{\langle \vec{\mu}(0)\vec{\mu}(t)\rangle}{\langle \vec{\mu}(0)\vec{\mu}(0)\rangle}, \quad (4)$$

obtained from the dipole moment time series of the NO molecule accumulated from a given trajectory. For further details on the calculation of infrared spectra, see Nutt and Meuwly (51).

RESULTS

Characterization of the ligand docking sites

The crystal structure of trHbN exhibits a continuous tunnel through the protein matrix with two perpendicularly placed channels. One end of each of the channels opens to the solvent while the other toward the heme. The entrance of the longer channel (channel I) is defined by residues Ile[19], Ile[25], Val[28], and Leu[102] whereas the entrance of the shorter channel (channel II) is surrounded by residues Phe[91],

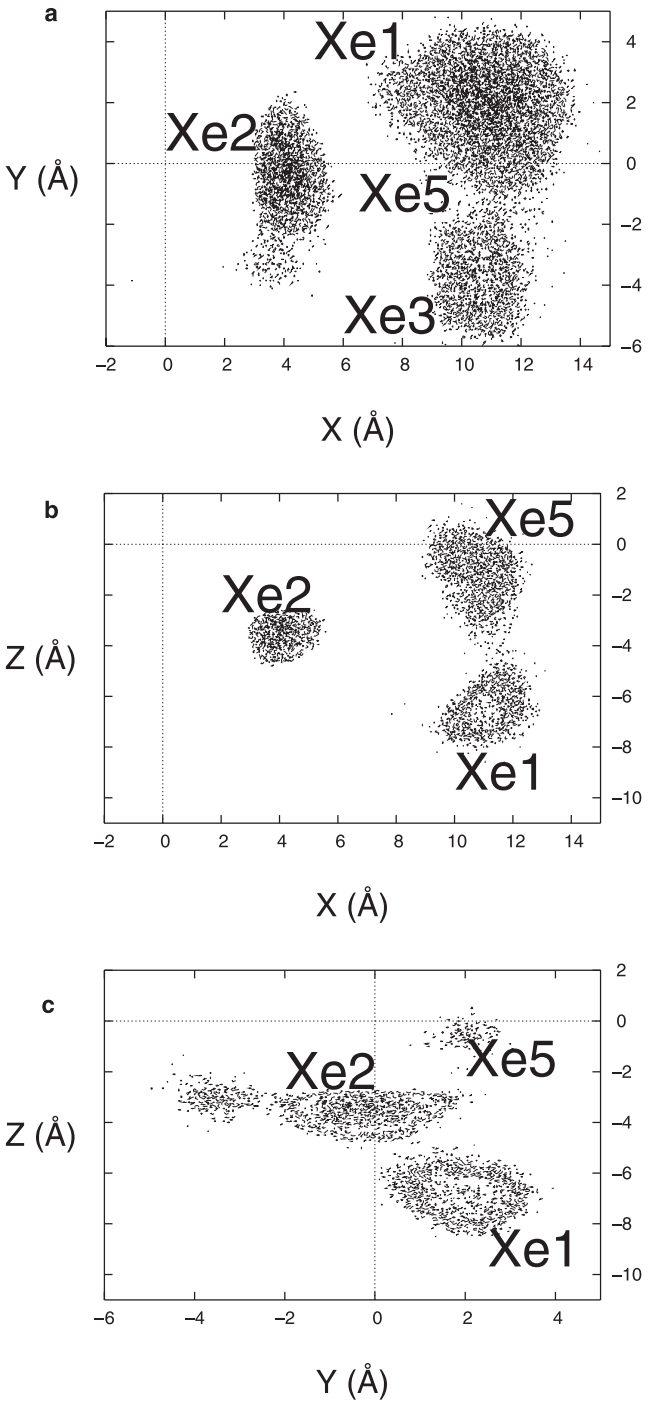

FIGURE 2 Contour plots in the *xy*-, *xz*-, and *yz* planes showing the probability distribution of the NO ligand from all the simulations. The heme plane is along the *xy* plane and the origin is shifted to the center of mass of the four N atoms of the porphyrin ring of the heme group. The ligand situated in different Xe pockets are labeled. The population of Xe4 pocket is too low to appear in the figure.

Ala[95], Leu[116], Ile[119], and Ala[120]. All residues defining the tunnel entrances and their inner surface are apolar. From Xe-pressurized protein samples three docking sites along channel II (the Xe2, Xe3, and Xe4 pockets) and two docking sites along channel I (the Xe1 and Xe5 pockets) were found

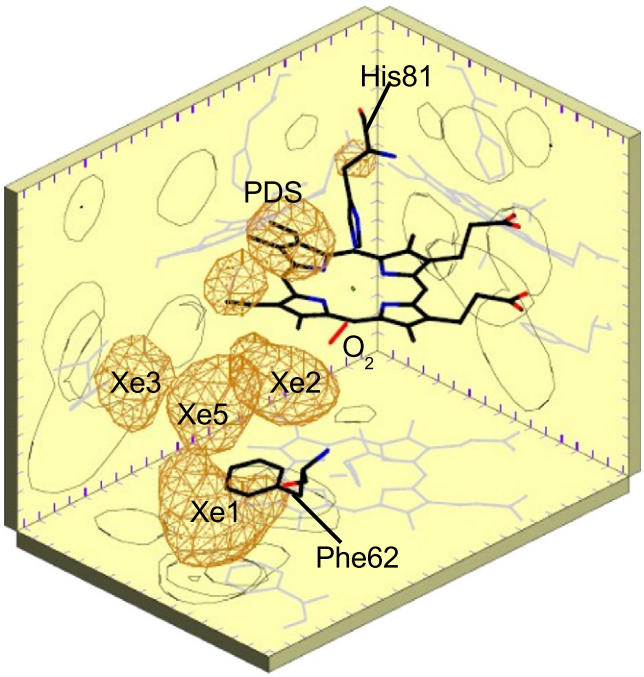

FIGURE 3 Three-dimensional view of the probability distribution of the NO ligand during the entire period of simulation. The heme group, proximal His[81], bound O_2, and Phe[62] are shown and the ligand docking sites are indicated. The population of Xe4 pocket is too low to appear in the figure. The figure is prepared using Surfplot software (67).

(12). In addition to these five Xe pockets, these simulations reveal the presence of an additional stable docking site (called proximal docking site: PDS) situated in the proximal side of the heme group in trHbN. A schematic diagram showing the Xe pockets and the PDS site in the trHbN is given in Fig. 1.

The cumulative probability distribution of the NO molecule in the three Cartesian planes from all 24 trajectories is shown in Fig. 2. The average heme plane is in the *xy* plane and the origin is at the center of mass of the four N atoms of the porphyrin ring of the heme group. In the two-dimensional projection of the ligand density distribution, some of the ligand docking sites overlap. In the *xy* plane, the Xe2 pocket (due to its proximity to the heme group) and the Xe3 pocket can be distinguished from other pockets. However, a distinction between the Xe1 and Xe5 pockets is difficult in the *xy* plane. In the *xz* plane, however, the Xe1 and Xe5 pockets can be differentiated. The spatial proximity of the Xe2 and the Xe1 pocket is best seen in the *yz* plane (Fig. 2).

For a spatial description of the probability distribution of the NO ligand from all simulations, Fig. 3 shows a three-dimensional probability density of the NO ligand in trHbN shown in its crystal structure conformation. While the density of the ligand is shown by mesh, the heme group, the bound O_2, the proximal His[81], and the Phe[62] residues are shown by sticks. In the three-dimensional projection, the ligand docking sites as well as their relative positions

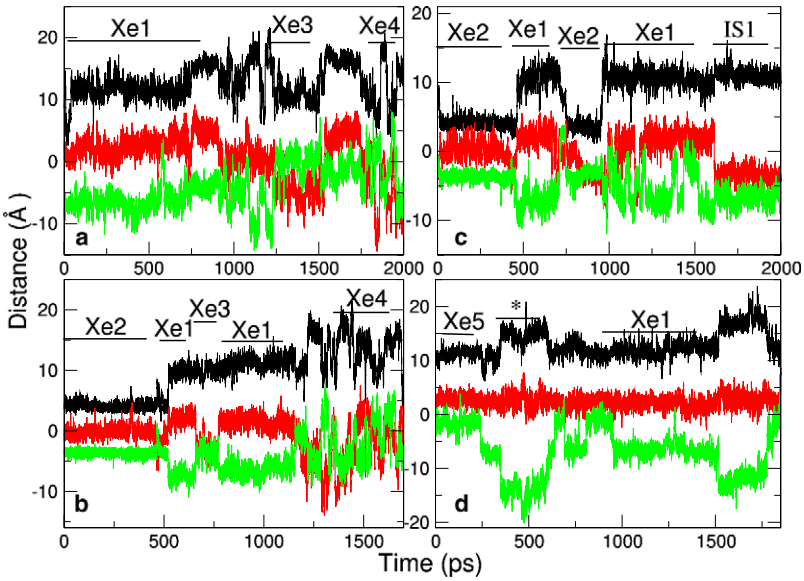

FIGURE 4 Time evolution of the *x*-, *y*-, and *z* coordinates (from *top* to *bottom* at time $t = 0$) of the position vector of N atom of the NO ligand, with respect to the center-of-mass of the four N atoms of the porphyrin ring of the heme group, in four trajectories chosen to illustrate ligand migration. The trajectories shown in panels *a–d* are started from snapshots with the NO ligand in the Xe1, Xe2, Xe3, and Xe5 pockets, respectively. The locations of the NO ligand during the simulations are marked in each of the figures. The intermediate site in between G and H helices is indicated by IS1 and the asterisk refers the ligand at the entrance of channel I.

and the degree of overlap with each other are discernible. In the distal side of the heme group, nearest to the bound O_2 ligand is the Xe2 pocket. The Xe5 and Xe1 pockets show overlapping density, which reflects the continuity of channel I. The Phe^{62} residue is situated between these two pockets. The region of the Xe1 pocket most distant from the heme plane corresponds to the entrance of channel I. The Xe4 pocket has negligible ligand density in these simulations, since the ligand upon arrival at the Xe4 pocket rapidly diffuses to bulk solvent via the opening of channel II. The Xe3 pocket is spatially close to the Xe2 and Xe5 pockets. The ligand docking site in the proximal side of the heme group and close to the His^{81} ring is the proximal pocket, which is not seen in crystallographic studies (11,12) and earlier simulations.

Fig. 4 shows the time evolution of the *x*-, *y*-, and *z* coordinates of the N atom of the NO molecule in four representative trajectories. For this purpose, the entire protein was reoriented so that the least-squares plane containing the four nitrogen atoms of the heme group lies in the *xy* plane, with the center-of-mass of the four nitrogen atoms placed at the origin. In the trajectory shown in Fig. 4 *a*, the NO ligand is initially in the Xe1 pocket. The ligand is found to move very rapidly from the Xe1 pocket to the Xe5 pocket and remains there briefly (for <10 ps) before returning to the Xe1 pocket. This process is completed within the first 50 ps of the simulation. Afterwards, the NO ligand remains in the Xe1 pocket for ~1 ns, then proceeds toward the Xe3 pocket via an intermediate site (IS1) between helices G and H (see Fig. 4 *b*). At ~1800 ps, the ligand migrates to the Xe4 pocket and further moves along channel II. In the trajectory shown in Fig. 4 *b*, the NO ligand starts in the Xe2 pocket. The ligand remains in the Xe2 pocket for ~500 ps and then proceeds to the Xe1 pocket. After this, rapid transitions between Xe1 and Xe3 pockets occur. Finally, via the intermediate site between helices G and H (IS1), the ligand moves to the Xe4 pocket and from there it escapes to the bulk water. In the example trajectory shown in Fig. 4 *c*, the ligand starts from the Xe3 pocket and rapidly moves toward the Xe2 pocket (along channel II). The ligand is then found to make several transitions between the Xe2 and Xe1 pockets. During the last 400 ps of the simulation, the ligand remains in IS1. In the last trajectory (Fig. 4 *d*) the ligand is initially in the Xe5 pocket and the ligand movement in this trajectory is primarily restricted to channel I (i.e., Xe5 and Xe1 pockets; see Fig. 4 *d*). In several of the calculated trajectories (i.e., 14 out of 24), the ligand escapes to the bulk solvent in <2 ns.

The primary ligand docking sites, their distance from the Fe atom of heme, the residues surrounding the docking sites, and the connectivity of the docking sites with other docking sites are given in Table 2.

The Xe1 pocket connects the Xe5 pocket with the entrance of channel I. Starting from the Xe1 pocket, the ligand migrates along three primary pathways: 1), to the Xe5 pocket; 2), toward the opening of channel I; or 3), toward the Xe3 pocket. The transfer of the ligand from the Xe1 pocket to the Xe5 pocket is assisted by the rotation of the phenyl ring of Phe^{62} residue. From Xe1 to Xe3, the ligand moves via the intermediate site (IS1) in between the helices G and H of trHbN. This intermediate site is surrounded by Ala^{95}, Leu^{98}, Ala^{99}, Ile^{112}, Ile^{115}, and Leu^{116} amino acids. The NO ligand is found to traverse this region of the protein, which connects the Xe1 pocket in channel I with the Xe3 and Xe4 pockets in channel II, in several trajectories.

Xe2 pocket is the closest docking site in the distal side of the heme group and hence is crucial for ligand rebinding and ligand chemistry such as oxidation of NO. Xe2 pocket is the intersection of channels I and II. Starting from the Xe2 pocket, the ligand can either move along channel II to the Xe3 pocket

TABLE 2 Ligand docking sites in trHbN of *Mycobacterium tuberculosis*

Pocket	Distance (Å)	Surrounding residues	Connectivity
Xe1	13	Phe^{62}, Ile^{25}, Ile^{115}, Val^{28}, Val^{29}, Leu^{98}	IS1, Xe5, Xe2, Xe3
Xe2	6	Phe^{32}, Leu^{98}, Ala^{94}, Phe^{62}, Tyr^{33}, Gln^{58}	Xe5, Xe3, Xe1, Solvent
Xe3	12	Phe^{62}, Leu^{98}, Leu^{66}, Ile^{115} Ile^{119}, Val^{118}, Ala^{65}	Xe1, Xe2, Xe4, IS1, Solvent
Xe4	15	Met^{88}, Phe^{91}, Ser^{92}, Ala^{95}, Gly^{96}, Ala^{123}	Xe3, IS1, Solvent
Xe5	9	Phe^{62}, Ala^{65}, Leu^{66}, Leu^{98}, Ile^{115}, Val^{118}	Xe1, Xe1, Solvent
PDS	6	Ile^{119}, Phe^{91}, His^{81}, Val^{124}, Ala^{123}, Asp^{125}, Val^{126}, Met^{77}	Xe2

The averaged distance of N atom of NO to Fe when NO is in a particular docking site of the protein is given in Å.

or along channel I to the Xe5 pocket. In addition, we also observed less frequent transitions from the Xe2 pocket to the Xe1 pocket. In some cases, the ligand from the stable Xe2 pocket was also found to move toward the C helix and escape to the bulk water via an exit pathway situated between helices C and F, and surrounded by Phe^{46}, Thr^{49}, Met^{51}, and Leu^{54} residues. The ligand remains in the Xe2 pocket for a longer period of time as compared to the other docking sites of the protein. This supports the proposal for multiligand chemistry taking place in the active site of the protein (16,52).

The Xe3 pocket, situated in the midway of channel II, has close access to bulk water and connects pockets Xe2 and Xe4. The ligand from the Xe3 pocket can move toward the Xe2 and Xe4 pockets along channel II or can move toward IS1 before reaching Xe1. In some cases, the ligand is found to move directly from the Xe3 pocket to the Xe1 pocket. Since the ligand spends typically a few tens of picoseconds in Xe3 pocket, this site is considered to be metastable. This is in agreement with the crystallographic observation that the Xe3 pocket is not a well-defined pocket in the A monomer of the trHbN dimer (12).

Starting from the Xe4 pocket, the ligand either moves along channel II toward the Xe3 pocket or escapes to the solvent. In addition to the movement along channel II, the ligand from Xe4 pocket is also seen to move toward IS1.

The Xe5 pocket is found in between the Xe1 and Xe2 pockets along channel I. From the Xe5 pocket, the ligand travels along channel I either toward the Xe1 pocket or toward the Xe2 pocket. Additionally, the ligand from the Xe5 pocket is also found to proceed to the bulk water via a region between the helices E and F, surrounded by Pro^{71}, Tyr^{72}, Phe^{62}, Ala^{65}, and Pro^{121} residues.

The PDS is extremely stable and the ligand exhibits no migration from this pocket during our 8 ns of simulation of the protein with NO in this pocket. The ligand in this docking site is surrounded by hydrophobic residues and has very little probability to escape the docking site.

Summarizing all ligand migration pathways from the simulations leads to a connectivity diagram for NO ligand transfer in trHbN, which is shown in Fig. 5. Although the apolar channels are the most preferred pathways for the ligand migration, the NO ligand does follow pathways in addition to the two channels, e.g., the transitions between Xe3/Xe2 and Xe1, and transitions between Xe4/Xe3 and Xe1 via IS1. There exist at least four different pathways via which the ligand can migrate through the protein to the bulk water. Two of these pathways are the openings of channels I and II, and the other two are the exit channels outside the tunnel of the protein (in between helices E and F and helices C and F).

Fig. 6 shows the free energy profile for the migration of the NO ligand in the trHbN protein matrix, estimated from the probability density of the Fe-N distance averaged over all the calculated trajectories as described in the previous section. The energy profile exhibits two distinct minima separated by a barrier of 1.2 kcal/mol. While the minimum at the lower value of Fe-N distance (~5 Å) corresponds to the Xe2 pocket and the proximal docking site of the protein, the broad minimum at the higher Fe-N distance corresponds to the Xe1, Xe3, and Xe5 pockets. These three pockets are indistinguishable in the free-energy profile along the Fe-N distance due to frequent transitions among these pockets that lead to a wide local minimum associated with the corresponding pockets, making an energetic distinction of these pockets along the Fe-N coordinate difficult. An energetically distinct characterization of individual docking sites can be achieved by nonequilibrium sampling methods such as umbrella sampling along some progression coordinates that can effectively distinguish the ligand docking sites.

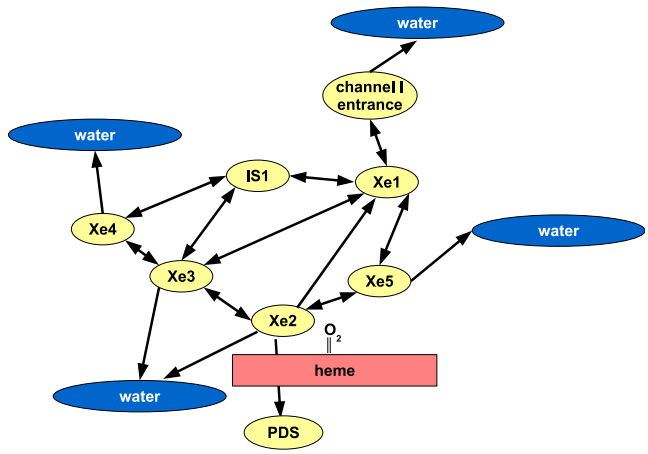

FIGURE 5 Connectivity network between the NO ligand docking sites within the trHbN protein matrix. The observed ligand transitions among various protein pockets are indicated by arrows. The loss of ligand to the bulk solvent is indicated by arrows toward water.

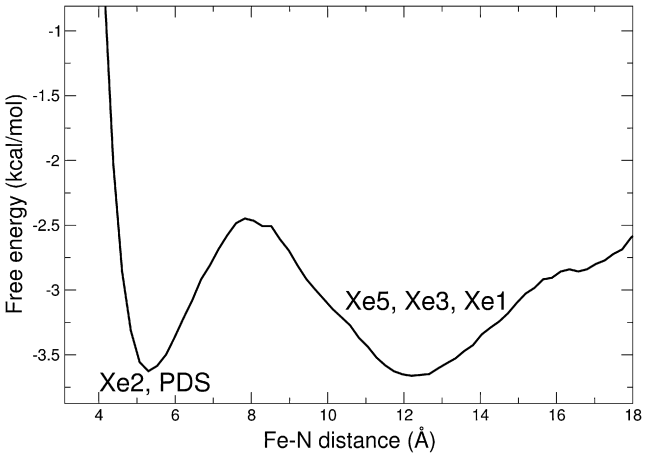

FIGURE 6 Free-energy profile for the migration of the NO ligand in the trHbN protein matrix. The progression coordinate is the distance between Fe atom of the heme and N atom of the NO ligand. The minimum at smaller Fe-N distance corresponds to the Xe2 pocket and the PDS, while the broad minimum at larger Fe-N separation corresponds to the Xe1, Xe3, and Xe5 pockets.

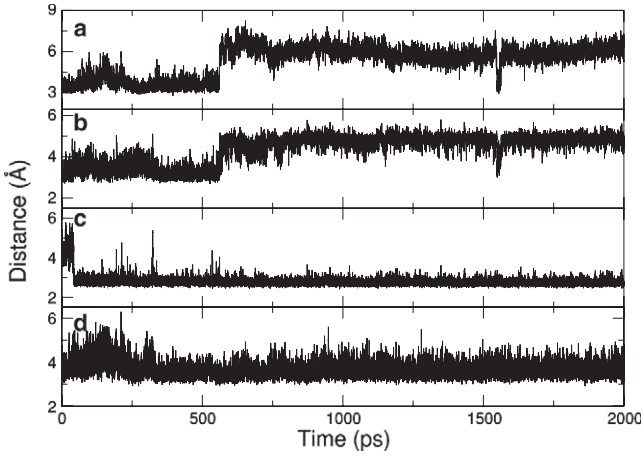

FIGURE 7 Time series of distances between (*a*) O2 of the bound O_2 and the phenolic O of the Tyr^{33}; (*b*) the phenolic O of the Tyr^{33} and the amide N of the Gln^{58}; (*c*) the phenolic O of the Tyr^{33} and the amide O of the Gln^{58}; and (*d*) O2 of the bound O_2 and the amide N of the Gln^{58}, for an example trajectory illustrating H-bonding pattern among Tyr^{33}, Gln^{58}, and the bound O_2 molecule.

H-bonding between O_2, Gln^{58}, and Tyr^{33}

The experimental spectroscopic and kinetic studies suggest the presence of an H-bonding network involving Tyr^{33}, Gln^{58}, and bound O_2 in the heme active site (15,17,18). Computational studies have been carried out to further characterize the H-bonding network in the heme active site for deoxy- and oxy-trHbN (28). In the following, we corroborate the experimental findings regarding the H-bonding network between the bound O_2 ligand and Tyr^{33} and Gln^{58} residues by analyzing the time evolution of their interactions and provide energetic estimates for these H-bonds. Fig. 7 illustrates the H-bonding pattern from a typical MD simulation and shows the time series of the distance between 1), the O2 atom (of O_2) and the phenolic O of the Tyr^{33}; 2), the amide N of the Gln^{58} and the phenolic O of the Tyr^{33}; 3), the phenolic O of the Tyr^{33} and the amide O of the Gln^{58}; and 4), the O2 of the bound O_2 and the amide N of the Gln^{58}, are given for such an example trajectory. Initially, H-bonds between the O2 and the phenolic O of the Tyr^{33}, and the phenolic O of the Tyr^{33} and the amide N of the Gln^{58}, are present (see Fig. 7 *a*). This situation is graphically illustrated in Fig. 8 *a*(*I*). After 60 ps, the phenolic O of the Tyr^{33} approaches the carbonyl O of the Gln^{58} (see the reduced bond distance in Fig. 7 *c*), leading to the breaking of the H-bond between the Tyr^{33} and the O2 atom and the formation of the H-bond between the amide O of the Gln^{58} and the phenolic O of the Tyr^{33} (shown in Fig. 8 *a*(*II*)). After $\approx$500 ps, the Tyr^{33} separates further from the O_2 ligand, while the amide group of Gln^{58} moves closer with the possibility to form an H-bond between the amide N of Gln^{58} and O2 of the bound O_2 (Fig. 7 *c*).

The free-energy profiles, associated with the H-bonded network calculated from all 24 trajectories, are shown in Fig. 8 *b*. It is seen that Tyr^{33} exhibits two conformations with respect to the bound O_2 ligand, regulating the H-bond between the phenolic O of Tyr^{33} and O_2. The energy barrier between the H-bonded Tyr^{33}-O_2 pair to the free Tyr^{33} and O_2 ligand is $\approx$1 kcal/mol. In contrast, the energy barrier to break the H-bonding between the phenolic O of the Tyr^{33} and carbonyl O of the Gln^{58} is $\approx$2 kcal/mol (see Fig. 8 *b*). As shown in Fig. 8 *a*, the amide group of Gln^{58} and the phenol ring of Tyr^{33} are found in three different conformations that also differ in their relative orientation. The minimum found at 3 Å corresponds to the situation where the amide O of Gln^{58} acts as an H-bond acceptor of the phenolic H of Tyr^{33} and the phenolic O of Tyr^{33} acts as an H-bond acceptor of the amide H of Gln^{58} (Fig. 8 *a*(*II*)). The intermediate minimum at 4.8 Å corresponds to the situation shown in Fig. 8 *a*(*I*), in which Tyr^{33} participates in H-bonding to the bound O_2 ligand as well as with the amide group of Gln^{58}. The conformation with the distance between the N atom of Gln^{58} and the O atom of Tyr^{33} at 6.5 Å reflects the situation where the amide group of Gln^{58} is engaged in H-bonding with O2 of the O_2 ligand and Tyr^{33} participates in the H-bonding with the amide O of Gln^{58} (Fig. 8 *a*(*III*)).

Phe^{62} controlled ligand migration along channel I

We have analyzed the trajectories calculated in this work to discuss the opening and closing of the Phe^{62} gate and its effects on the ligand migration. Similar to previous studies (11,12,27,28), we find the Phe^{62} residue exhibiting two conformations. In one of the conformations, the phenyl ring of the residue blocks the channel I while in the other it lets the ligand move along channel I. Our simulations revealed that the Phe^{62} residue in the oxy-trHbN exhibits

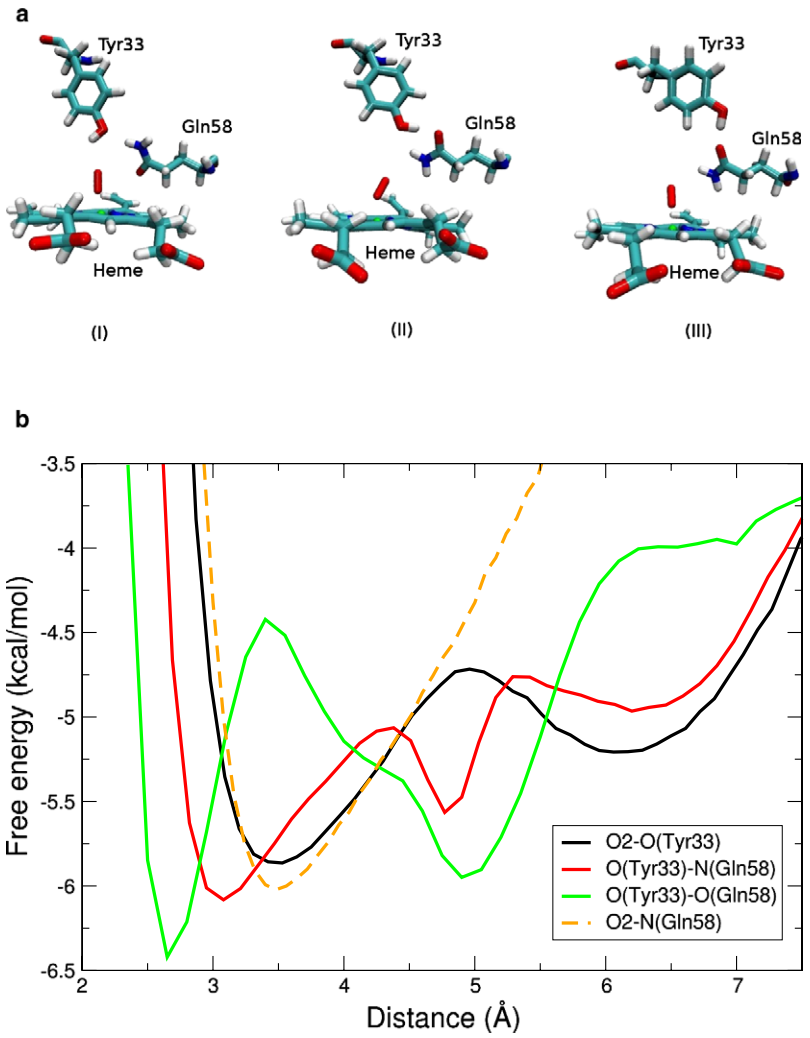

FIGURE 8 (*a*) Schematic representation of orientation of Tyr_{33}, Gln^{58}, and the bound O_2 molecule during the trajectory shown in Fig. 7. (*b*) Free-energy profiles for H-bonding among Gln^{58}, Tyr^{33}, and the bound O_2 molecule. (*Inset*) Progression coordinates associated with the energy curves.

primarily the open conformation (probability >70%), see Fig. 9 *a*, where the averaged probability distribution of the dihedral angle H_α-C_α-C_β-C_γ of Phe^{62} residue provides a comparison between the populations of the closed and open conformations. By analyzing individual trajectories, we found that the change in conformation is a less frequent event. The conformational change from an open state to a closed state is more rare than the opposite, indicating the presence of a larger energy barrier for an open-to-closed transition. This is verified from the free energy profile calculated for the ring torsion of the Phe^{62} residue. For the oxy-trHbN, the open state conformer is found 1.5 kcal/mol more stable than the closed conformer. The energy barrier for closed-to-open transition is ~1.2 kcal/mol whereas the reverse energy barrier is >3 kcal/mol (see Fig. 9 *b*). The barrier for ring torsion originates from a combination of 1), H-bond breaking and formation between Tyr^{33} and Gln^{58} residue pair; and 2), steric interactions between Phe^{62} and Gln^{58} residues.

To illustrate the ligand migration associated with the open-closed transition of the Phe^{62} residue, we present an example trajectory in Fig. 9, *c* and *d*, where the ligand movement and Phe^{62} ring torsion are visibly correlated. The time series of the dihedral angle H_α-C_α-C_β-C_γ of Phe^{62} is plotted in Fig. 9 *c* and the time series of the *x*-, *y*-, and *z* coordinates of the NO ligand in the trajectory is plotted in Fig. 9 *d*. (The ligand transition between the Xe5 and the Xe1 pockets is indicated by the *vertical dashed lines* in Fig. 9, *c* and *d*.) During this simulation, the phenyl ring adopts both closed and open conformations and during the first nanosecond of the simulation, three transitions occur between the two conformations. The ligand is initially found in the Xe5 pocket, where it stays for ~240 ps before it moves along channel I toward the Xe1 pocket. During the transition of the ligand from the Xe5 pocket to the Xe1 pocket, the Phe^{62} residue exhibits open conformation and soon after the transition, the residue adopts the closed conformation (see Fig. 9 *c* at 300 ps). The ligand remains in the Xe1 pocket for next 250 ps, during which the Phe^{62} remains in the closed conformation. At ~475 ps, Phe^{62} adopts the open conformation and 5 ps later, the ligand moves along the open channel toward Xe5 pocket. This example trajectory clearly

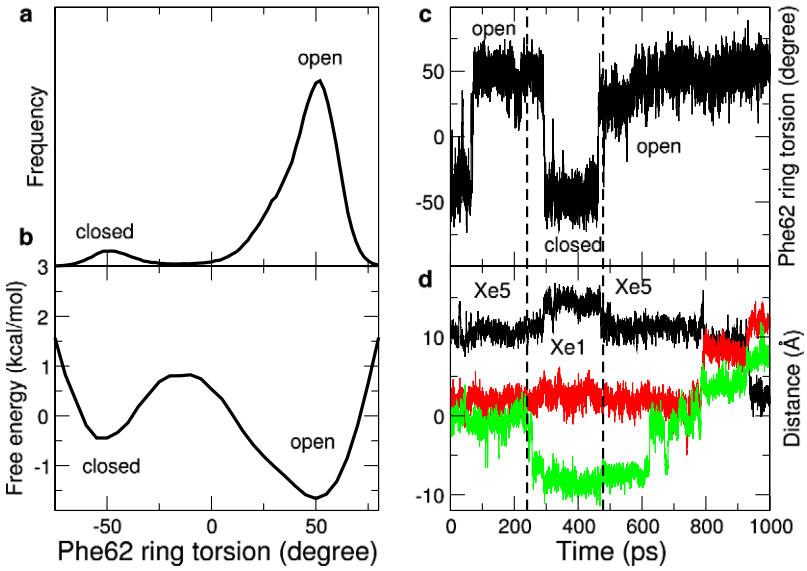

FIGURE 9 (*a*) Average probability distribution of the conformations of the dihedral angle H_α-C_α-C_β-C_γ of Phe^{62} residue in oxy-trHbN. (*b*) Free-energy profile associated with the ring torsion of the Phe^{62} residue. The dihedral angle of $-50°$ and $+50°$ corresponds to the open and closed states of the Phe^{62} residue, which refer to the situations when the phenyl ring of Phe^{62} residue blocks and unblocks, respectively, the passage between the Xe5 and Xe1 pockets along channel I. Time series of (*c*) Phe^{62} phenyl ring torsion and (*d*) *x*-, *y*-, and *z* coordinates of the NO ligand in an example trajectory to illustrate the correlation between the movement of Phe^{62} and ligand migration. The vertical dashed lines at 240 ps and 480 ps indicate the migration of the ligand from the Xe5 to the Xe1 pocket and the reverse migration, respectively.

demonstrates the ligand migration being controlled by the change in the Phe^{62} conformation.

Infrared spectra of NO in trHbN

The harmonic (ω_e) and the fundamental (ν_e) frequency associated with a Morse potential (Eq. 1) are given by

$$\omega_e = \hbar\beta\sqrt{\frac{2D_e}{\mu}},$$
$$\nu_e = \hbar\beta\left[\sqrt{\frac{2D_e}{\mu}} - \frac{\hbar\beta}{\mu}\right]. \quad (5)$$

With the Morse potential used in this work, the analytic fundamental and harmonic frequencies of NO are (ν_e) 1798.8 cm^{-1} and (ω_e) 1830.1 cm^{-1}, respectively. To investigate the performance of the Morse potential used for N-O bond in the MD simulations, we calculated the infrared spectrum of an isolated NO molecule in vacuum. The resulting spectrum shows a sharp peak at 1837.5 cm^{-1}. The difference of 39 cm^{-1} compared to the calculated fundamental frequency (ν_e) is consistent with the previous investigations for similar systems (51,53) and is related to two factors: 1), the classical treatment of the Morse potential; and 2), the use of Verlet integrator with the time step of 1 fs employed to integrate the equations of motion in the MD simulations (51,53). The experimental gas phase infrared spectrum of NO shows absorption at 1875.9 cm^{-1} (50). In myoglobin, the infrared spectrum of photodissociated NO exhibits two peaks at 1857 and 1867 cm^{-1} and spreads over a spectral window of 10–30 cm^{-1} between 1840 and 1880 cm^{-1} (39,42).

The infrared spectrum of NO in the protein environment averaged over all 24 individual trajectories is broad with extended tails to both sides of the central, most intense feature, and exhibits several peaks as shown in Fig. 10 *a*. It spans over a spectral region of 20 cm^{-1} between 1830 and 1850 cm^{-1}, centered around the gas phase NO absorption peak at 1837.5 cm^{-1} (see *dashed line* in Fig. 10 *a*). The averaged infrared spectrum shows an intense peak at 1837.5 cm^{-1} with a shoulder at 1839 cm^{-1}. Two additional peaks with moderate-to-high intensity are seen to the red (at 1835.5 cm^{-1}) and blue (at 1840.5 cm^{-1}) side of the central peak. The position, relative intensity, and width of six Gaussian functions fitted to the spectral features of Fig. 10 *a* are given in Table 3.

Fig. 10 *b* shows NO-infrared spectra from four trajectories, which differ in the ligand sampling particular regions

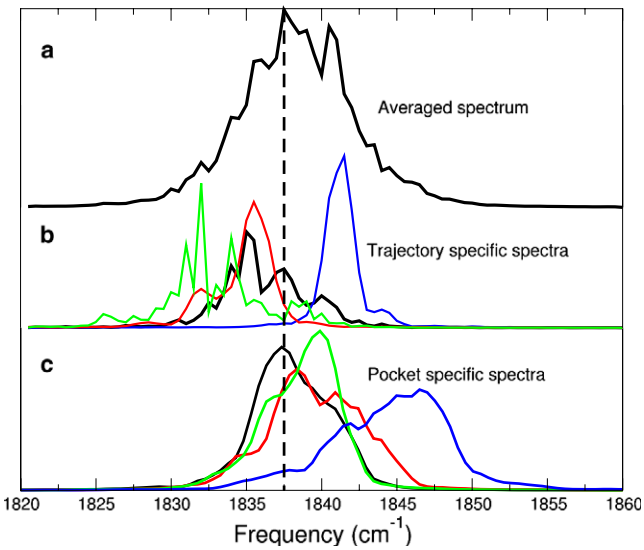

FIGURE 10 (*a*) Infrared spectrum of NO ligand averaged over 24 spectra calculated from individual trajectories. (*b*) NO infrared spectra from four trajectories, which differ in the regions of protein sampled by the ligand. (*c*) Averaged infrared spectra of NO in the Xe1 (*black*), Xe2 (*red*), Xe5 (*green*), and the proximal pocket (*blue*). The absorption of NO molecule in the gas phase is indicated by the dashed line at 1837.5 cm^{-1}.

TABLE 3 Position, intensity, and full width at half-maximum (FWHM) of the Gaussian functions describing the profile of the averaged infrared spectrum of NO in trHbN (shown in Fig. 10 *a*)

Frequency (cm^{-1})	Intensity (%)	FWHM
1834.3	45.5	1.97
1835.8	75.5	2.05
1837.5	100.0	3.14
1838.9	90.0	1.88
1840.6	92.3	2.88
1842.0	52.0	3.16

inside the protein. The black line is an infrared spectrum calculated from a trajectory where NO primarily remains in the Xe1 and Xe5 pockets, with occasional migration to Xe3. The red spectrum corresponds to a trajectory in which NO migrates between Xe2 and Xe4, whereas the broad and structured green spectrum corresponds to a trajectory in which the NO molecule migrates between Xe5 and Xe1, and the entrance of channel I. Finally, the blue spectrum in Fig. 10 *b* arises from a trajectory with the NO molecule in Xe2. This information alone is not sufficient to assign particular spectral features to specific pockets sampled. To this end, Fig. 10 *c* shows the averaged NO spectra when the ligand movement is restricted to a given ligand docking site. Such docking-site specific spectra provide a means for a spectroscopic identification of ligand docking sites in a protein. To achieve this, we collected the time series of the dipole moments of NO from those parts of trajectories where the ligand was localized in a given docking site from which pocket-specific spectra were obtained. By averaging over all such pocket-specific spectra from different trajectories, we obtained averaged infrared spectrum of NO ligand in particular docking sites. Since the ligand was not found in the Xe3 and the Xe4 for a sufficiently long time to calculate meaningful pocket-specific infrared spectra, the analysis is only carried out for Xe1, Xe2, Xe5, and the proximal docking site (see Fig. 10 *c*). By combining the information from Fig. 10, *b* and *c*, the following assignments are proposed: for NO in the Xe1 pocket, an infrared absorption occurs at 1837.5 cm^{-1} (i.e., unshifted with respect to free NO), whereas the infrared absorption of the ligand in the Xe5 pocket leads to signals at 1835 and 1841 cm^{-1}. The ligand in Xe2 pocket shows three distinct absorption maxima located at 1834, 1839, and 1842 cm^{-1}. The ligand in Xe3 or Xe4 pocket shows red-shifted absorption (at <1834 cm^{-1}). Finally, for the NO molecule in the PDS, a blue-shifted broad infrared peak at 1847 cm^{-1} is found. In conclusion, the infrared spectrum for unbound NO inside truncated hemoglobin is expected to exhibit a relatively broad (≈ 20 cm^{-1}) spectrum with largely unresolved bands centered around the absorption of free NO. For a spectroscopic characterization of the ligand docking sites, however, site-specific infrared spectra need to be recorded. This may also include investigation of suitably mutated proteins to block particular ligand migration pathways.

DISCUSSION AND CONCLUSIONS

By using the ligand as a probe, the present simulations have characterized the internal structure of trHbN including active site conformation, ligand migration pathways, ligand docking sites, and solvent-accessible regions. The connectivity network given in Fig. 5 shows the possible transition pathways of the ligand within the protein matrix. The tunnel system of trHbN plays an important role in determining and controlling ligand entrance, migration, and rebinding. The ligand is also seen to follow migration pathways besides the tunnel, for example, migration from Xe1 and Xe3 pocket via IS1 (see Fig. 5). In addition to the five Xe pockets found in the crystallographic study of Milani et al. (12), the present simulations find another ligand docking site in the proximal side of the heme group in trHbN. The simulations reveal four different regions of the protein from which the ligand can escape the protein matrix to the bulk water. Two of these pathways are the openings of channel I and II, surrounded by apolar residues. The other two exit channels fall outside the tunnel of the protein, accessible from the Xe2 and Xe5 pockets. While the exit pathway close to the Xe5 pocket lies between helices E and F (surrounded by Pro^{71}, Tyr^{72}, Phe^{62}, Ala^{65}, and Pro^{121} residues), the exit path close to the Xe2 pocket is situated between the helices C and F (surrounded by Phe^{46}, Thr^{49}, Met^{51}, and Leu^{54}). Both of these extratunnelar exit paths are surrounded by at least one polar residue, e.g., Thr, Pro, or Tyr. The exit channels surrounded by polar residues are expected to be the preferred escape channel for charged or highly polar ligands. Recently, a study involving the release of NO_3^- (the product of NO detoxification) from the heme distal side to solvent finds that the polar nitrate anion does not escape the protein via the well-characterized apolar tunnels. Instead, the anion prefers a path close to the Met^{51} and Thr^{49} residues in between helices C and F (54).

The above discussion opens the possibility for competing ligand-migration pathways operating in the protein matrix. A nonpolar ligand, such as O_2, prefers protein channels delineated by apolar residues. On the contrary, a highly polar ligand, such as the nitrate anion (NO_3^-), follows exit pathways surrounded by polar residues. The three-point fluctuating charge model, employed in this work for NO, correctly describes the strong quadrupole moment of the ligand. Therefore, NO represents an intermediate case, where the ligand is neither apolar nor highly polar. In such a case, a competition between polar and nonpolar pathways is possible, as is seen in this work (see Fig. 5).

Other recent studies exploring the interior of oxy-trHbN were carried out with a grid-based MD method for fast and unsupervised exploration of protein channels (55). In this method, a precomputed grid of forces for protein conformations interact with the rigid probe (ligand). Although such an approach is computationally efficient, it ignores the influence of the ligand on the protein dynamics, which, in the present

work, is found to be important. Consequently, this study, although it reports the presence of the exit pathway between E and F helices, failed in locating the proximal docking site, the intermediate site (IS1) between Xe1 and Xe3 pocket, and the nonpolar exit pathway (between C and F helices), shown to exist in the present work. All experimentally and computationally characterized pathways are found from a single computational model in the present study, which is not the case for previous simulations (28,54,55). The additional exit channels are expected to be important for removing the products of NO detoxification reaction from the protein matrix. Although our simulations are not sufficiently long to capture the reentrance of the NO ligand from bulk to protein, by observing four exit routes of the ligand, we anticipate that the ligand can also enter the protein matrix via these pathways. This can be verified by running long simulations with ligand outside the protein matrix. The increased number of access routes of the ligand should also increase the probability of capturing nitric oxide for efficient detoxification.

Most likely, the novel observations of the proximal docking site as well as the exit channels, besides the tunnel openings, are consequences of using an accurate electrostatic model for the ligand. The Xe pockets and tunnel branches observed from crystallographic studies suggest possible ligand migration sites within and through the protein (56). However, other and additional sites might be found from atomistic simulations. The interactions between protein residues and the ligand mutually influence their dynamics and may open additional localization sites and migration pathways. This has been previously shown for myoglobins (35,57), and this study is an additional example. In this context, it should be noted that simulations, in which the ligand location is determined implicitly from the classical molecular interaction potential (as in (27,28,52,55)), are liable to failure in capturing the novel phenomena that arise solely due to explicit interaction of the ligand with the fluctuating protein.

In this work, the presence, energetics, and dynamics of the active-site hydrogen-bonding network has been characterized explicitly. The resonance Raman spectrum of the oxy-trHbN shows the Fe-O_2 stretching mode at 562 cm^{-1} (17,18). Upon mutation of the Tyr^{33} to Leu^{33}, this peak shifted to 540 cm^{-1}, which is the Fe-O_2 stretching frequency observed in most other hemoglobins and myoglobins (17,18). One possible reason for this observation is the presence of an H-bonding between Tyr^{33} and the bound O_2 ligand. Furthermore, a red shift of the Fe-O_2 stretching frequency was seen upon Gln^{58}Val mutation, indicating an H-bond between the bound O_2 and the Gln^{58} residue (17,18). Finally, the kinetic and equilibrium constants for the reaction of ferrous HbN with O_2 compared to those of other proteins reveal that the O_2 binding is twofold faster in trHbN compared to sperm whale Mb, whereas O_2 dissociation is two-orders-of-magnitude slower in trHbN. This is because of the presence of a tunnel in the trHbN for a faster ligand diffusion to the heme active site and the presence of a ligand-stabilizing residue (Tyr^{33}) restricting ligand dissociation (15). The spectroscopic and kinetic studies thus suggest the presence of an H-bonding network in the heme active site. Previously, the existence of such a network has been indirectly characterized through Tyr^{33}Phe and Gln^{58}Ala mutational studies (28).

The present simulations show the presence of a dynamic H-bonding network between the bound O_2 ligand and Tyr^{33} and Gln^{58} residues. From detailed analysis of the residue movements, it is concluded that the phenolic O of Tyr^{33} plays the role of both H-bond donor and acceptor with the amide N of Gln^{58}. Additionally, the phenolic O of Tyr^{33} also participates as an H-bond donor to the amide O of Gln^{58}. This is in contrast to previous results (28) where, from one 50-ns trajectory for oxy-trHbN, it was found that Tyr^{33} acts exclusively as H-bond acceptor of the amide H of Gln^{58} and as H-bond donor to bound O_2. On the contrary, our simulations suggest that the O_2 ligand acts as H-bond acceptor of both the phenolic H of Tyr^{33} as well as the amide H of Gln^{58}, and the H-bond between Tyr^{33} and O_2 is dynamic in nature. Three different conformations arising from the mutual H-bonds between these moieties have been identified (see Fig. 8 *a*) and energetic estimations of the involved H-bonds have been provided (Fig. 8 *b*). While the breaking of H-bond between O_2 and Tyr^{33} pertains a barrier of 1.2 kcal/mol, the barriers involving the breaking of H-bonds between Tyr^{33} and amide N and amide O of Gln^{58} amounts to 1 kcal/mol and 2 kcal/mol, respectively. The H-bonds among these moieties are frequently formed and broken during simulations. The small energy barriers indicate that the H-bonds in the heme active site are not energy-demanding. The dynamic H-bonds involving small energy requirements support the ligand chemistry that takes place in the heme active site. Since the stability and mobility of the intermediates and the products of the NO detoxification process depend on the surrounding residues, the low energy barriers are desirable for accommodation of different reactive conformations that may play a role in the detoxification reaction.

The Phe^{62} residue situated in the helix E of the trHbN lies in a strategic position to control the ligand migration between Xe5 and Xe1 pockets along channel I. From crystallographic studies it is known that Phe^{62} adopts two conformations, differing by a rotation around the C_α-C_β bond (11,12). This aspect has been further studied by MD simulations (27,28). By comparing the energy barriers associated with ligand migration along the two channels, a dual path mechanism has been postulated, stating that O_2 enters the deoxy-trHbN from channel II, while NO enters the oxy-trHbN from channel I (27,28). The present simulations substantiate this observation with additional facts such as energy barrier between the two conformations and direct observation of the role of the Phe^{62} in ligand migration. We have estimated the energy barrier for closed-state-to-open-state transition as

1.2 kcal/mol, whereas the reverse energy barrier is ≈3 kcal/mol. Owing to the larger barrier, open-to-closed transition is less frequent than the opposite. Our simulations revealed that the open state of the Phe^{62} residue is prevalent in the case of oxy-trHbN. It has been found that ligand migration between pockets Xe1 and Xe5 along the channel I is correlated to a conformational change of the Phe^{62} residue. The role of Phe^{62} in trHbN as a gate controlling the ligand migration along channel I is reminiscent of His^{64} in myoglobin, where no permanent channel exists in the molecular structure of the protein that connects the active site to the outside, but an outward movement of the His^{64} imidazole side chain may transiently open a pathway through which ligands may enter or exit the distal heme cavity (58–61).

Using an anharmonic potential for the bond-stretching and accurate electrostatic interactions including higher multipole moments, for several diatomic ligands (such as CO, CN^-, and NO) in myoglobin, it has been shown that the experimentally observed splittings of the ligand absorption spectrum can be understood from MD simulations (51,53, 62–64). The averaged infrared spectra of NO, calculated in this work (Fig. 10 *a*), is broad and extends over a spectral window of 20 cm^{-1} with a central intense peak at 1837.5 cm^{-1}. The averaged spectrum is broad with tails at both sides of the maximum and exhibits several splittings; these are typically 1.5–2 cm^{-1}. The considerable width of the spectrum is in qualitative agreement with the experimental infrared spectrum of NO in myoglobin (39,42), where both blue and red shifts of the central intense peak are observed. Similar to this spectra (see Fig. 10 *a*), the experimental spectra of dissociated NO in myoglobin (39,42) are broad and structured with peaks separated by a few wave numbers. As for photodissociated CO in myoglobin, these peaks most likely correspond to conformational substates which, however, have not yet been unambiguously assigned.

In addition to the averaged infrared spectra of NO, the individual spectra arising from trajectories, where ligand samples different regions of protein, are also analyzed. In recent years with the development of experimental techniques, it is now possible to record infrared spectra of ligands in specific ligand docking sites and spectroscopically characterize the docking sites of the protein (65,66). This has also been achieved in this computational work where pocket-specific NO infrared spectra have been calculated. By comparing the spectra shown in Fig. 10, *a–c*, the following attempt to correlate structure and spectroscopy is made: The central part of the averaged spectrum originates from NO in Xe1, Xe2, and Xe5, which are buried inside the protein and close to the heme active site. The peaks toward the red side of the averaged spectrum are primarily due to the ligand in Xe3, Xe4, and the opening of channel I. These positions are away from the heme active site and close to the surrounding bulk solvent, which gives rise to the red-shifted peaks. On the other hand, the blue-shifted tail of the averaged infrared spectrum is primarily due to the ligand in the proximal pocket, which consists of hydrophobic residues such as Ile^{119}, Phe^{91}, His^{81}, Val^{124}, Val^{126}, Ala^{123}, Met^{77}, and Asp^{125}. The polar side chain of Asp^{125} lies close to the surrounding solvent molecules and away from the proximal docking site, thus keeping the proximal docking site hydrophobic. The contribution of the Xe3, Xe4, and the proximal docking sites to the overall spectrum is expected to be rather minimal, whereas the overall spectrum is expected to be dominated by the ligand located in Xe1, Xe2, and Xe5.

In summary, we have studied nitric oxide migration in the trHbN of *M. tuberculosis* via molecular-dynamics simulation, by using a fluctuating three-point charge model and a Morse potential for the NO molecule. By analyzing the ligand probability density, we have characterized the primary ligand docking sites in the protein matrix. In addition to the five Xe pockets found in the crystallographic study of Milani et al. (12), our simulations find another ligand docking site on the proximal side of the heme group in trHbN. By studying the ligand dynamics, a connectivity network could be determined that describes transition pathways of the ligand in the protein matrix including novel migration pathways and exit channels. A structural and energetic account of dynamic H-bonding network (among Tyr^{33}, Gln^{58}, and bound O_2) operating in the heme active site has been found and characterized and the pivotal role of Phe^{62} in ligand migration has been confirmed. Finally, the simulations allow prediction of the (site-specific) infrared spectra of NO in trHbN, which as yet have not been observed experimentally. The different bands of the infrared spectrum have been assigned through comparison with pocket-specific infrared spectra of NO ligand and it will be interesting to compare these findings with experiments.

The authors thank Mr. Christian Wäckerlin for helpful discussions.

Financial support from the Swiss National Science Foundation is gratefully acknowledged.

REFERENCES

1. Kundu, S., J. T. Trent, and M. S. Hargrove. 2003. Plants, humans, and hemoglobins. *Trends Plant Sci.* 8:387–393.
2. Garrocho-Villegas, V., S. K. Gopalasubramaniam, and R. Arredondo-Peter. 2007. Plant hemoglobins: what we know six decades after their discovery. *Gene*. 398:78–85.
3. Vuletich, D. A., and J. T. Lecomte. 2006. A phylogenetic and structural analysis of truncated hemoglobins. *J. Mol. Evol.* 62:196–210.
4. Wittenberg, J. B., M. Bolognesi, B. A. Wittenberg, and M. Guertin. 2002. Truncated hemoglobins: a new family of hemoglobins widely distributed in bacteria, unicellular eukaryotes, and plants. *J. Biol. Chem.* 277:871–874.
5. Milani, M., A. Pesce, M. Nardini, H. Ouellet, Y. Ouellet, et al. 2005. Structural bases for heme binding and diatomic ligand recognition in truncated hemoglobins. *J. Inorg. Biol. Chem.* 99:97–109.
6. Pesce, A., M. Nardini, M. Milani, and M. Bolognesi. 2007. Protein structure in the truncated (2/2) hemoglobin family. *IUBMB Life*. 59:535–541.
7. Nardini, M., A. Pesce, M. Milani, and M. Bolognesi. 2007. Protein fold and structure in the truncated (2/2) globin family. *Gene*. 398:2–11.

8. Ascenzi, P., M. Bolognesi, M. Milani, M. Guertin, and P. Visca. 2007. Mycobacterial truncated hemoglobins: from genes to functions. *Gene*. 398:42–51.
9. Ascenzi, P., and P. Visca. 2008. Scavenging of reactive nitrogen species by mycobacterial truncated hemoglobins. *Methods Enzymol*. 436: 317–337.
10. Pesce, A., M. Milani, M. Nardini, and M. Bolognesi. 2008. Mapping heme-ligand tunnels in group I truncated (2/2) hemoglobins. *Methods Enzymol*. 436:303–315.
11. Milani, M., A. Pesce, Y. Ouellet, P. Ascenzi, M. Guertin, et al. 2001. *Mycobacterium tuberculosis* hemoglobin N displays a protein tunnel suited for O_2 diffusion to the heme. *EMBO J*. 20:3902–3909.
12. Milani, M., A. Pesce, Y. Ouellet, S. Dewilde, J. Friedman, et al. 2004. Heme-ligand tunneling in group I truncated hemoglobins. *J. Biol. Chem.* 279:21520–21525.
13. Kochi, A. 1991. The global tuberculosis situation and the new control strategy of the World Health Organization. *Tubercle*. 72:1–6.
14. Bloom, B. R. 1994. Tuberculosis: Pathogenesis, Protection, and Control. ASM Press, Washington, DC.
15. Couture, A., S.-R. Yeh, B. A. Wittenberg, J. B. Wittenberg, Y. Ouellet, et al. 1999. A cooperative oxygen-binding hemoglobin from *Mycobacterium tuberculosis*. *Proc. Natl. Acad. Sci. USA*. 96:11223–11228.
16. Ouellet, H., Y. Ouellet, C. Richard, M. Labarre, B. Wittenberg, et al. 2002. Truncated hemoglobin HbN protects *Mycobacterium bovis* from nitric oxide. *Proc. Natl. Acad. Sci. USA*. 99:5902–5907.
17. Yeh, S.-R., M. Couture, Y. Ouellet, M. Guertin, and D. L. Rousseau. 2000. A cooperative oxygen binding hemoglobin from *Mycobacterium tuberculosis* stabilization of heme ligands by a distal tyrosine residue. *J. Biol. Chem.* 275:1679–1684.
18. Ouellet, Y., M. Milani, M. Couture, M. Bolognesi, and M. Guertin. 2006. Ligand interactions in the distal heme pocket of *Mycobacterium tuberculosis* truncated hemoglobin N: roles of Tyr^{B10} and Gln^{E11} residues. *Biochemistry*. 45:8770–8781.
19. Mukai, M., Y. Ouellet, H. Ouellet, M. Guertin, and S.-R. Yeh. 2004. NO binding induced conformational changes in a truncated hemoglobin from *Mycobacterium tuberculosis*. *Biochemistry*. 43:2764–2770.
20. Milani, M., Y. Ouellet, H. Ouellet, M. Guertin, A. Boffi, et al. 2004. Cyanide binding to truncated hemoglobins: a crystallographic and kinetic study. *Biochemistry*. 43:5213–5221.
21. Poole R. K., editor. 2008. Globins and Other Nitric Oxide-Reactive Proteins, Part A. Vol. 436 Academic Press, New York.
22. Poole R. K., editor. 2008. Globins and Other Nitric Oxide-Reactive Proteins, Part B. Vol. 437 Academic Press, New York.
23. Tamir, S., S. Burney, and S. R. Tannenbaum. 1996. DNA damage by nitric oxide. *Chem. Res. Toxicol*. 9:821–827.
24. Angelo, M., A. Hausladen, D. Singel, and J. S. Stamler. 2008. Interactions of NO with hemoglobin: from microbes to man. *Methods Enzymol*. 436:131–168.
25. Goldstein, S., and G. Merenyi. 2008. The chemistry of peroxynitrite: implications for biological activity. *Methods Enzymol*. 436:49–61.
26. Nutt, D., M. Karplus, and M. Meuwly. 2005. Potential energy surface and molecular dynamics of MbNO: existence of an unsuspected FeON minimum. *J. Phys. Chem. B*. 109:2118–2125.
27. Bidon-Chanal, A., M. A. Martí, A. Crespo, M. Milani, M. Orozco, et al. 2006. Ligand-induced dynamical regulation of NO conversion in *Mycobacterium tuberculosis* truncated hemoglobin-N. *Proteins*. 64:457–464.
28. Bidon-Chanal, A., M. A. Martí, D. A. Estrin, and F. J. Luque. 2007. Dynamical regulation of ligand migration by a gate-opening molecular switch in truncated hemoglobin-N from *Mycobacterium tuberculosis*. *J. Am. Chem. Soc*. 129:6782–6788.
29. Frauenfelder, H. 1981. Structural fluctuations in proteins. *Eur. Biophys. J*. 7:226–227.
30. Brunori, M., F. Cutruzzola, C. Savino, C. Travaglini-Allocatelli, B. Vallone, et al. 1999. Does picosecond protein dynamics have survival value? *Trends Biochem. Sci*. 24:253–255.
31. Šrajer, V., T. Y. Teng, T. Ursby, C. Pradervand, Z. Ren, et al. 1996. Photolysis of the carbon monoxide complex of myoglobin: nanosecond time-resolved crystallography. *Science*. 274:1726–1729.
32. Šrajer, V., Z. Ren, T. Y. Teng, M. Schmidt, T. Ursby, et al. 2001. Protein conformational relaxation and ligand migration in myoglobin: a nanosecond to millisecond molecular movie from time-resolved Laue x-ray diffraction. *Biochemistry*. 40:13802–13815.
33. Schotte, F., M. Lim, T. A. Jackson, A. V. Smirnov, J. Soman, et al. 2003. Watching a protein as it functions with 150-ps time-resolved x-ray crystallography. *Science*. 300:1944–1947.
34. Schmidt, M., K. Nienhaus, R. Pahl, A. Krasselt, S. Anderson, et al. 2005. Ligand migration pathway and protein dynamics in myoglobin: a time-resolved crystallographic study on L29W MbCO. *Proc. Natl. Acad. Sci. USA*. 102:11704–11709.
35. Cohen, J., A. Arkhipov, R. Braun, and K. Schulten. 2006. Imaging the migration pathways for O_2, CO, NO, and Xe inside myoglobin. *Biophys. J*. 91:1844–1857.
36. Champion, P. M., F. Rosca, D. Ionascu, W. Cao, and X. Ye. 2004. Rapid timescale processes and the role of electronic surface coupling in the photolysis of diatomic ligands from heme proteins. *Faraday Discuss*. 127:123–135.
37. Moncada, S., R. Palmer, and E. Higgs. 1991. Nitric oxide: physiology, pathophysiology, and pharmacology. *Pharmacol. Rev*. 43:109–142.
38. Ionascu, D., F. Gruia, X. Ye, A. Yu, F. Rosca, et al. 2005. Temperature-dependent studies of NO recombination to heme and heme proteins. *J. Am. Chem. Soc*. 127:16921–16934.
39. Miller, L. M., A. J. Pedraza, and M. R. Chance. 1997. Identification of conformational substates involved in nitric oxide binding to ferrous and ferric myoglobin through difference Fourier transformed infrared spectroscopy (FTIR). *Biochemistry*. 36:12199–12207.
40. Park, E. S., M. R. Thomas, and S. G. Boxer. 2000. Vibrational Stark spectroscopy of NO bound to heme: effects of protein electrostatic fields on the NO stretch frequency. *J. Am. Chem. Soc*. 122:12297–12303.
41. Coyle, C. M., K. M. Vogel, T. S. Rush III, P. M. Kozlowski, R. Williams, et al. 2003. FeNO structure in distal pocket mutants of myoglobin based on resonance Raman spectroscopy. *Biochemistry*. 42:4896–4903.
42. Nienhaus, K., P. Palladino, and G. U. Nienhaus. 2008. Structural dynamics of myoglobin: FTIR-TDS study of NO migration and binding. *Biochemistry*. 47:935–948.
43. Nutt, D., and M. Meuwly. 2004. Ligand dynamics in myoglobin: calculation of infrared spectra for photodissociated NO. *ChemPhysChem*. 5:1710–1718.
44. Brooks, B., R. Bruccoleri, B. Olafson, D. States, S. Swaminathan, et al. 1983. CHARMM: a program for macromolecular energy, minimization, and dynamics calculations. *J. Comput. Chem.* 4:18–217.
45. Jorgensen, W. L., J. Chandrasekhar, J. D. Madura, R. W. Impey, and M. L. Klein. 1983. Comparison of simple potential functions for simulating liquid water. *J. Chem. Phys.* 79:926–935.
46. MacKerell, Jr., A. D., D. Bashford, M. Bellott, J. R. L. Dunbrack, et al. 1998. All atom empirical potential for molecular modeling and dynamics studies of proteins. *J. Phys. Chem. B*. 102:3586–3616.
47. Steinbach, P. J., and B. R. Brookes. 1994. New spherical-cutoff methods for long-range forces in macromolecular simulation. *J. Comput. Chem.* 15:667–683.
48. van Gunsteren, W., and H. Berendsen. 1977. Algorithms for macromolecular dynamics and constraint dynamics. *Mol. Phys.* 34:1311–1327.
49. Meuwly, M., O. M. Becker, R. Stone, and M. Karplus. 2002. NO rebinding to myoglobin: a reactive molecular dynamics study. *Biophys. Chem.* 98:183–207.
50. Herzberg, G. 1950. Molecular Spectra and Molecular Structure: Spectra of Diatomic Molecules. Van Nostrand Reinhold, New York.
51. Nutt, D., and M. Meuwly. 2003. Theoretical investigation of infrared spectra and pocket dynamics of photodissociated carbonmonoxy myoglobin. *Biophys. J*. 85:3612–3623.

52. Crespo, A., M. A. Martí, S. G. Kalko, A. Morreale, M. Orozco, et al. 2005. Theoretical study of the truncated hemoglobin HbN: exploring the molecular basis of the NO detoxification mechanism. *J. Am. Chem. Soc.* 127:4433–4444.

53. Danielsson, J., and M. Meuwly. 2007. Molecular dynamics simulations of CN^- dynamics and spectroscopy in myoglobin. *Chem. Phys. Chem.* 8:1077–1084.

54. Martí, M. A., A. Bidon-Chanal, A. Crespo, S. -R. Yeh, V. Guallar, et al. 2008. Mechanism of product release in NO detoxification from *Mycobacterium tuberculosis* truncated hemoglobin N. *J. Am. Chem. Soc.* 130:1688–1693.

55. Carrillo, O., and M. Orozco. 2008. GRID-MD—a tool for massive simulation of protein channels. *Proteins.* 70:892–899.

56. Brunori, M., and Q. Gibson. 2001. Cavities and packing defects in the structural dynamics of myoglobin. *EMBO Rep.* 2:676–679.

57. Huang, X., and S. G. Boxer. 1994. Discovery of new ligand binding pathways in myoglobin by random mutagenesis. *Nat. Struct. Biol.* 1:226–229.

58. Perutz, M. F. 1989. Myoglobin and hemoglobin: role of distal residues in reactions with heme ligands. *Trends Biochem. Sci.* 14:42–44.

59. Johnson, K. A., J. S. Olson, and G. N. Phillips Jr. 1989. Structure of myoglobin-ethyl isocyanide. Histidine as a swinging door for ligand entry. *J. Mol. Biol.* 207:459–463.

60. Zhu, L., J. T. Sage, A. A. Rigos, D. Morikis, and P. M. Champion. 1992. Conformational interconversion in protein crystals. *J. Mol. Biol.* 224:207–215.

61. Yang, F., and G. N. Phillips, Jr. 1996. Crystal structures of CO-, deoxy-, and met-myoglobins at various pH values. *J. Mol. Biol.* 256:762–774.

62. Nutt, D., and M. Meuwly. 2004. CO migration in native and mutant myoglobin: atomistic simulations for the understanding of protein function. *Proc. Natl. Acad. Sci. USA.* 101:5998–6002.

63. Nutt, D., and M. Meuwly. 2007. Ferric and ferrous iron in nitrosomyoglobin: computer simulations of stable and metastable states and their infrared spectra. *ChemPhysChem.* 8:527–536.

64. Plattner, N., and M. Meuwly. 2008. The role of higher CO-multipole moments in understanding the dynamics of photodissociated carbon monoxide in myoglobin. *Biophys. J.* 94:2505–2515.

65. Sato, A., Y. Gao, T. Kitagawa, and Y. Mizutani. 2007. Primary protein response after ligand photodissociation in carbonmonoxy myoglobin. *Proc. Natl. Acad. Sci. USA.* 104:9627–9632.

66. Nienhaus, K., and G. U. Nienhaus. 2008. Influence of distal residue B10 on CO dynamics in myoglobin and neuroglobin. *J. Biol. Phys.* 10.1007/s10867-008-9059-2.

67. Laskowski, R. A. 1995. SURFNET: a program for visualizing molecular surfaces, cavities, and intermolecular interactions. *J. Mol. Graph.* 13:323–330.